Journal of Fluids and Structures 25 (2009) 897–917

JOURNAL OF
FLUIDS AND
STRUCTURES

www.elsevier.com/locate/jfs

High fidelity computational simulation of a membrane wing airfoil

R.E. Gordnier*

AFRL/RBAC, Bldg 146 Rm 225, 2210 Eighth St, Wright-Patterson AFB, OH 45433-7512, USA

Received 25 April 2008; accepted 15 March 2009
Available online 19 May 2009

Abstract

Computations and analysis for a two-dimensional flexible membrane wing airfoil are presented. A well-validated, robust, sixth-order Navier–Stokes solver is employed coupled with a membrane structural model suitable for the highly nonlinear structural response of the membrane. A low Reynolds number, Re = 2500, consistent with MAV flight is chosen for the majority of the calculations. The most notable effect of the membrane flexibility is the introduction of a mean camber to the membrane airfoil. A close coupling between unsteady vortex shedding and the dynamic structural response is demonstrated. The dynamic motion of the membrane surface is also shown to significantly alter the unsteady flow over the membrane airfoil at high angles of attack. The coupling of this dynamic effect and the mean camber results in a delay in stall with enhanced lift for higher angles of attack. Exploratory computations investigating the effects of angle of attack, membrane rigidity, membrane pretension and Reynolds number on the membrane airfoil response are also presented.
Published by Elsevier Ltd.

Keywords: Membrane wing; Micro air vehicle; Wing stall; Vortex shedding

1. Introduction

In order to address the technical challenges associated with successful MAV development, designers are looking to biological flight for inspiration. Successful development of these biomimetic MAV concepts will require significant advancements in the fundamental understanding of the unsteady aerodynamics of low Reynolds number fliers and the associated fluid–structure interactions. The inherent flexibility in the structural design of lightweight MAVs and the exploitation of that flexibility creates strong coupling between the unsteady fluid dynamics and the airframe structural response, giving rise to tightly integrated, multidisciplinary physics. Conventional simplified analytical techniques and empirical design methods, although attractive for their efficiency, may have limited applicability for these complicated, multidisciplinary design problems. Critical insight into the highly complex, coupled MAV physics calls for the exploitation of advanced multidisciplinary computational techniques.

Recent MAV designs have attempted to exploit wing flexibility by employing membrane wings (Shyy et al., 2005). Flexible membrane wings offer the potential to better adapt to stall arising from gusts and maneuvers and may allow for beneficial aeroelastic tailoring and active control. Previous work on membrane wings has been motivated by the

---

*Tel.: +1 937 904 4051; fax: +1 937 656 7867.
E-mail address: raymond.gordnier@wpafb.af.mil

0889-9746/$ - see front matter Published by Elsevier Ltd.
doi:10.1016/j.jfluidstructs.2009.03.004

study of sails. Newman (1987) provides a review of this work which is predominantly based on steady inviscid, incompressible flow theory. Newman and Païdoussis (1991) have also investigated the stability of two-dimensional membranes at small incidences. An inviscid, unsteady flow model has been developed and applied to the study of harmonic perturbations of the trailing edge of sails and random inflow velocities by Le Maitre et al. (1999). In order to understand the complex flow interactions engendered by low Reynolds number membrane wing MAVs, higher-fidelity viscous aeroelastic solvers are required to capture the relevant physical phenomena.

The focus of the present paper will be the viscous aeroelastic simulation and analysis of aeroscience issues associated with a flexible membrane wing airfoil. Previous computations by Smith and Shyy (1995) and Shyy and Smith (1997) have investigated the response of a membrane airfoil to an unsteady free stream. More recently Persson et al. (2007) have investigated both fixed and oscillating membrane airfoils using a high-order discontinuous Galerkin method. Experimental flow visualizations as well as PIV measurements have been carried out by Rojratsirikul et al. (2008) for a simple membrane wing. Song and Breuer (2007) have also investigated experimentally the dynamics of compliant membrane wings as related to mammalian flight.

In this paper computations of a flexible membrane wing will be performed using a well validated, robust, sixth-order Navier–Stokes solver (Gaitonde and Visbal, 1998, 1999; Visbal and Gaitonde, 1999) coupled with a membrane structural model (Smith and Shyy, 1995) suitable for the highly nonlinear structural response associated with a membrane airfoil. This same flow solver has been coupled with other linear and nonlinear structural models to investigate panel flutter (Gordnier and Visbal, 2002; Visbal and Gordnier, 2004) and the aeroelastic response of flexible delta wings (Gordnier and Visbal, 2004; Attar and Gordnier, 2006). For the low Reynolds numbers considered in this paper, both the fluid flow and structural response are assumed to be two-dimensional. The impact of various fluid and structural parameters including angle of attack, membrane elasticity, membrane pretension and Reynolds number are explored. Comparisons with computations for corresponding rigid membrane airfoils will be made to highlight the positive impact of structural flexibility and dynamic motion.

2. Aerodynamic solver

2.1. Governing equations

The governing equations solved are the two-dimensional, compressible Navier–Stokes equations. These equations are cast in strong conservative form introducing a general time-dependent curvilinear coordinate transformation $(x, z, t) \rightarrow (\xi, \zeta, \tau)$. In vector notation, and employing nondimensional variables, the equations are

$$\frac{\partial}{\partial \tau}\left(\frac{\vec{U}}{J}\right) + \frac{\partial \hat{F}}{\partial \xi} + \frac{\partial \hat{H}}{\partial \zeta} = \frac{1}{\mathrm{Re}}\left[\frac{\partial \hat{F}_v}{\partial \xi} + \frac{\partial \hat{H}_v}{\partial \zeta}\right]. \tag{1}$$

Here $\vec{U} = \{\rho, \rho u, \rho w, \rho E\}$ denotes the solution vector and J is the transformation Jacobian. The inviscid and viscous fluxes, $\hat{F}, \hat{H}, \hat{F}_v$ and $\hat{H}_v$ can be found, for instance, in Anderson et al. (1984). In the expressions above, u and w are the Cartesian velocity components, ρ the density, p the pressure, and T the temperature. All flow variables have been normalized by their respective freestream values except for pressure which has been nondimensionalized by $\rho_\infty u_\infty^2$. The system of equations is closed using the perfect gas law $p = \rho T / \gamma M_\infty^2$, Sutherland's formula for viscosity, and the assumption of a constant Prandtl number, $\mathrm{Pr} = 0.72$.

2.2. Spatial discretization

A finite-difference approach is employed to discretize the flow equations. For any scalar quantity, ϕ, such as a metric, flux component or flow variable, the spatial derivative ϕ' along a coordinate line in the transformed plane is obtained by solving the tridiagonal system

$$\alpha \phi'_{i-1} + \phi'_i + \alpha \phi'_{i+1} = b\frac{\phi_{i+2} - \phi_{i-2}}{4} + a\frac{\phi_{i+1} - \phi_{i-1}}{2}, \tag{2}$$

where $\alpha = \frac{1}{3}$, $a = \frac{14}{9}$, $b = \frac{1}{9}$ and $i = 1, \ldots IL$ with IL being the maximum grid dimension along the coordinate line. This choice of coefficients yields at interior points the compact five-point, sixth-order algorithm of Lele (1992). At boundary points 1, 2, $IL - 1$ and IL, fourth- and fifth-order one-sided formulas are utilized which retain the tridiagonal form of the interior scheme (Gaitonde and Visbal, 1998; Visbal and Gaitonde, 1998).

Compact-difference discretizations, like other centered schemes, are nondissipative and are therefore susceptible to numerical instabilities due to the growth of spurious high-frequency modes. These difficulties originate from several sources including mesh nonuniformity, approximate boundary conditions and nonlinear flow features. In order to ensure long-term numerical stability, while retaining the improved accuracy of the spatial compact discretization, a high-order implicit filtering technique (Gaitonde et al., 1997; Visbal and Gaitonde, 1999) is incorporated. If a component of the solution vector is denoted by ϕ, filtered values $\hat{\phi}$ are obtained by solving the tridiagonal system

$$\alpha_f \hat{\phi}_{i-1} + \hat{\phi}_i + \alpha_f \hat{\phi}_{i+1} = \sum_{n=0}^{N} \frac{a_n}{2} (\phi_{i+n} + \phi_{i-n}). \tag{3}$$

Eq. (3) is based on templates proposed in Lele (1992) and Alpert (1981), and with proper choice of coefficients, provides a $2N$th-order formula on a $2N+1$ point stencil. The coefficients, $a_0, a_1, \dots a_N$, derived in terms of the single parameter α_f using Taylor- and Fourier-series analysis, are given in Gaitonde and Visbal (1998), along with detailed spectral filter responses. In the present study, an eighth-order filter operator with $\alpha_f = 0.3$ is applied at interior points. For near-boundary points, the filtering strategies described in Visbal and Gaitonde (1999) and Gaitonde and Visbal (1999) are employed. Filtering is applied to the conserved variables, and sequentially in each coordinate direction.

2.3. Time integration

For wall-bounded viscous flows, the stability constraint of explicit time-marching schemes is too restrictive and the use of an implicit approach becomes necessary. For this purpose, the implicit approximately factored scheme of Beam and Warming (1978) is incorporated and augmented through the use of Newton-like subiterations in order to achieve second-order temporal and sixth-order spatial accuracy. In delta form, the scheme may be written as

$$\begin{aligned} &\left[J^{-1^{p+1}} + \phi^i \Delta\tau \delta_\xi^{(2)} \left(\frac{\partial \hat{F}^p}{\partial U} - \frac{1}{\mathrm{Re}} \frac{\partial \hat{F}_v^p}{\partial U} \right) \right] J^{p+1} \left[J^{-1^{p+1}} + \phi^i \Delta\tau \delta_\zeta^{(2)} \left(\frac{\partial \hat{H}^p}{\partial U} - \frac{1}{\mathrm{Re}} \frac{\partial \hat{H}_v^p}{\partial U} \right) \right] \Delta U \\ &\quad = -\phi^i \Delta\tau \left[J^{-1^{p+1}} \frac{(1+\phi)U^p - (1+2\phi)U^n + \phi U^{n-1}}{\Delta\tau} + U^p (1/J)_\tau^p + \delta_\xi \left(\hat{F}^p - \frac{1}{\mathrm{Re}} \hat{F}_v^p \right) + \delta_\zeta \left(\hat{H}^p - \frac{1}{\mathrm{Re}} \hat{H}_v^p \right) \right], \end{aligned} \tag{4}$$

where

$$\phi^i = \frac{1}{1+\phi}, \quad \Delta U = U^{p+1} - U^p. \tag{5}$$

For the first subiteration, $p = 1$, $U^p = U^n$ and as $p \to \infty$, $U^p \to U^{n+1}$. Either first- or second-order temporal accuracy can be prescribed by specifying $\phi = 0$ or $\frac{1}{2}$, respectively. The spatial derivatives in the implicit (left-hand side) operators are represented using standard second-order centered approximations, whereas high-order discretizations are employed for the explicit terms (right-hand side). Although not shown in Eq. (4), nonlinear artificial dissipation terms (Jameson et al., 1981; Pulliam, 1986) are appended to the implicit operator to enhance stability. In addition, for improved efficiency, the approximately factored scheme is recast in diagonalized form (Pulliam and Chaussee, 1981). Any degradation in solution accuracy caused by the second-order implicit operators, artificial dissipation and the diagonal form are eliminated through the use of subiterations. Typically, three subiterations are applied per time step.

2.4. Boundary conditions

The boundary conditions for the flow domain are prescribed as follows. At the solid surface, the no slip condition is applied, requiring that the fluid velocity at the wing surface match the surface velocity. In addition, the adiabatic wall condition, $\partial T/\partial n = 0$, and the normal pressure gradient condition $\partial p/\partial n = 0$ are specified. Along the O-grid cut, spatial periodicity is imposed by means of a grid overlap region.

The treatment of the farfield boundaries is based on the approach proposed and evaluated previously in Visbal and Gaitonde (2001) for some acoustic benchmark problems. This method exploits the properties of the high-order, low-pass filter in conjunction with a rapidly stretched mesh. As grid spacing increases away from the region of interest, energy not supported by the stretched mesh is reflected in the form of high-frequency modes which are annihilated by the discriminating spatial filter operator. An effective "buffer" zone is therefore created using a few grid points in each coordinate direction to rapidly stretch to the farfield boundary. No further need for the explicit incorporation of complicated boundary conditions or modifications to the governing equations is then required. Freestream conditions are specified along the inflow portion of the farfield boundary, while simple extrapolation of all variables is used on the outflow portion of the boundary.

3. Membrane airfoil solver

3.1. Governing equation

The structural model employed for the membrane is based on the model presented by Smith and Shyy (1995) for a one-dimensional nonlinear membrane subjected to a normal force. The governing equation in nondimensional form is

$$\rho_s h \frac{d^2 z}{dt^2} + \rho_s C_d \frac{dz}{dt} - T \frac{d^2 z}{dx^2} \left[1 + \left(\frac{dz}{dx} \right)^2 \right]^{-3/2} = \Delta p, \tag{6}$$

where

$$T = Eh(\delta_0 + \bar{\delta}), \tag{7}$$

$$\bar{\delta} = L - 1, \tag{8}$$

and

$$L = \int_0^1 \sqrt{1 + \left(\frac{dz}{dx} \right)^2}\, dx. \tag{9}$$

In these equations ρ_s, h, C_d, T, E and δ_0 are the membrane density, thickness, damping, tension, modulus of elasticity and the length increase of the pretensed membrane, respectively. These quantities have been nondimensionalized by the freestream density, dynamic pressure, and chord length of the airfoil or a combination thereof.

3.2. Numerical solver

To develop the numerical solution procedure for the membrane structural equation, Eq. (6) is rewritten as a system of two equations, as follows:

$$\frac{dz}{dt} - v_s = 0, \tag{10}$$

$$\rho_s h \frac{dv_s}{dt} + C_d v_s - T \left[1 + \left(\frac{dz}{dx} \right)^2 \right]^{-3/2} \frac{d^2 z}{dx^2} = \Delta p. \tag{11}$$

Eq. (11) is linearized by computing the term $T[1 + (dz/dx)^2]^{-3/2}$ at the previous subiteration. The pressure force which comes from the coupling with the aerodynamic solver is also assumed known from the previous subiteration. The temporal derivatives in Eqs. (10) and (11) are computed using a second-order accurate three-point backward stencil while the spatial derivatives are computed using second-order accurate central differences. Any degradation in the solution accuracy due to the linearization of Eq. (11) and the lagging of the pressure term is eliminated via subiterations which are also used in the solution of the aerodynamic equations. The membrane is assumed to be pinned at the two ends with no deflections allowed.

4. Aerodynamic/structural coupling

Coupling of the aerodynamics with the membrane response occurs through the imposed pressure force, Δp, in Eq. (6) and by the resulting deflection of the membrane, which is returned to the aerodynamic grid. Implicit coupling of these two sets of equations is achieved by a global subiteration strategy. During each subiteration the aerodynamic forces in the membrane equations are updated and the new surface displacements are provided to the aerodynamic solver. Using this approach the temporal lag between the aerodynamic and membrane equations may be eliminated and a complete synchronization of the aerodynamic/structural equation set is achieved. This synchronization of the fluid and structures solution is essential in eliminating spurious long-term instabilities which may arise from nonsychronized or lagged approaches to coupling (Gordnier and Visbal, 2002). Any factorization or linearization errors introduced in the equations may also be eliminated using this global subiteration procedure. The resulting coupled procedure retains second-order temporal accuracy.

When solving fluid/structure interactions, the aerodynamic mesh must be allowed to move in accordance with the motion of the structural surface. A simple algebraic method described in Melville et al. (1997) deforms the aerodynamic mesh to accommodate the changing membrane surface position. This grid motion strategy has proved adequate for the membrane motions considered in the present work.

5. Results

The membrane airfoil geometry computed is based on the experimental model of Rojratsirikul et al. (2008), Fig. 1. In these experiments the membrane wing consists of a thin latex sheet stretched between two small, aerodynamically shaped, rigid mounts. The membrane is glued to the mounts which results in pinned boundary condition for the flexible membrane. Experimental observations (Rojratsirikul et al., 2008) indicate a membrane deformation that is essentially one-dimensional and a two-dimensional, laminar flow is assumed for the low Reynolds numbers considered here. An O-type mesh consisting of 409 points around the membrane airfoil and 151 points in the normal direction (50–60 points located in the boundary layer region) is developed. One hundred and one points are distributed along the upper and lower surfaces of the flexible membrane with a maximum spacing of $\Delta x = 0.0149$. Around the leading and trailing edge mounts 103 grid points are employed. The minimum spacing at the wall is $\Delta z_{\min} = 0.0001$ and the grid stretches to the outer boundary located 100 chords from the airfoil.

Table 1 gives the fluid and structural dynamic parameters for each of the cases computed. The structural parameters are representative of a latex membrane type wing. Each computation assumes a mass ratio, $\rho_s h = 0.589$, and no

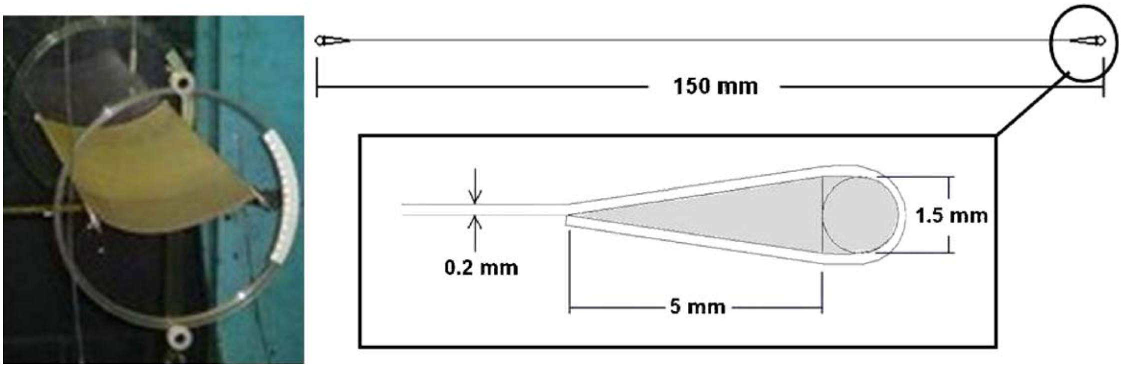

Fig. 1. Membrane wing geometry of Rojratsirikul et al. (2008).

Table 1
Fluid and structure nondimensional parameters for computed cases.

Case	α	Reynolds number	Eh	δ_0	$\rho_s h$
1	4	2500	50	0.0	0.589
2	8	2500	50	0.0	0.589
3	12	2500	50	0.0	0.589
4	16	2500	50	0.0	0.589
5	20	2500	50	0.0	0.589
6	8	2500	25	0.0	0.589
7	8	2500	100	0.0	0.589
8	8	2500	50	0.01	0.589
9	8	2500	50	0.02	0.589
10	8	5000	50	0.0	0.589
11	8	10 000	50	0.0	0.589

structural damping, $C_d = 0$. The flow is essentially incompressible with a freestream Mach number, $M_\infty = 0.05$ specified. The coupling of the aerodynamic and structural dynamic equations introduces a rich parameter space to be explored. Computations are performed over an angle of attack range $\alpha = 4$–20° (Cases 1–5, Table 1) to study changes associated with increasing incidence. The influence of membrane rigidity is investigated by varying the elasticity parameter, *Eh* (Cases 2, 6, 7). Similarly, how membrane pretension alters the membrane behavior is examined by progressively increasing the amount of the pretension (Cases 2, 8, 9). Finally, computations are performed to determine how the flow and structural dynamics of the membrane transform for Reynolds numbers ranging from $\mathrm{Re} = 2500$ to 10 000 (Cases 2, 10, 11). For all cases the mean response will be examined first followed by a description of the corresponding unsteady results.

5.1. Effect of angle of attack

5.1.1. Mean response

Fig. 2 displays the mean vorticity and streamline patterns for angles of attack ranging from $\alpha = 4^\circ$ to 20°. The most obvious effect of the membrane flexibility is the development of a mean camber to the airfoil. Fig. 3(a), which plots the mean surface deflection for each angle of attack, shows the evolution of this camber. The maximum deflection grows over the incidence range considered from $z_{\max} = 0.0724$ at $\alpha = 4^\circ$ to $z_{\max} = 0.0899$ at $\alpha = 20^\circ$. At $\alpha = 4^\circ$ the membrane shape is nearly symmetric. It becomes progressively more asymmetric with the point of maximum deflection moving upstream as the incidence increases up to $\alpha = 16^\circ$ where the maximum deflection is located at $x = 0.426$. As angle of attack is increased further, the point of maximum deflection starts to move back downstream.

Fig. 2 shows the impact of increasing angle of attack and the corresponding mean camber on the flowfield. At $\alpha = 4^\circ$ the flow separates at $x = 0.738$ resulting in a narrow separation bubble extending to the trailing edge, Fig. 2(f). A very small separation bubble is noted upstream with separation occurring from the rigid membrane mount and attaching on the membrane surface at $x = 0.036$. It should be noted that the rigid membrane mount used in the experiment directly influences the structure of the upstream separation, with separation always occurring from the rigid mount. This fact suggest that how the underlying support structure for a membrane is designed may have direct consequences for the

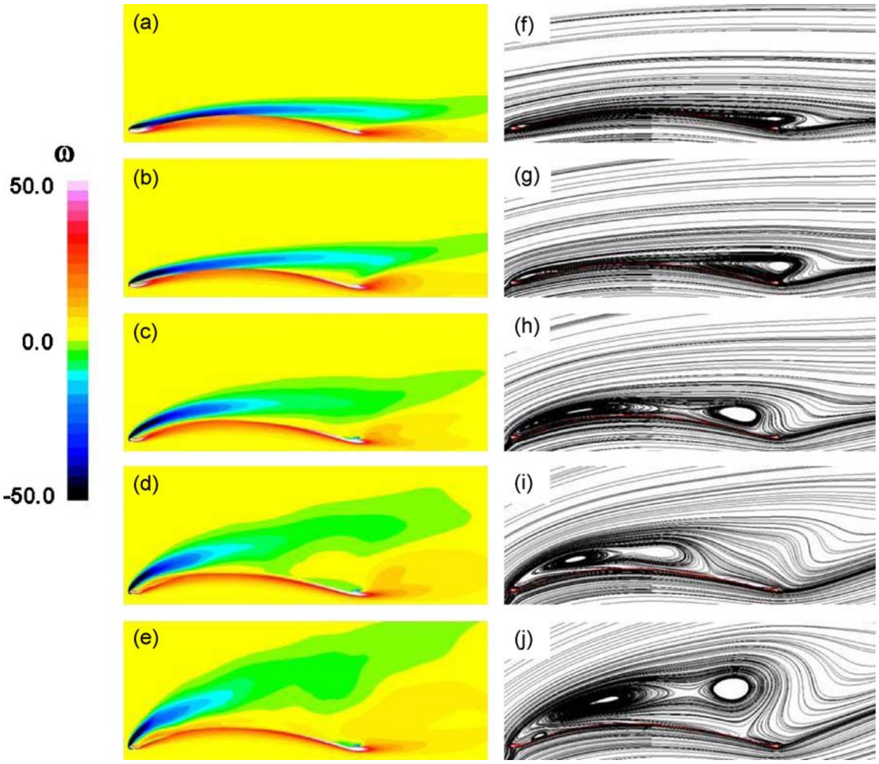

Fig. 2. Mean vorticity and streamline patterns for various angles of attack: (a, f) $\alpha = 4^\circ$, (b, g) $\alpha = 8^\circ$, (c, h) $\alpha = 12^\circ$, (d, i) $\alpha = 16^\circ$, (e, j) $\alpha = 20^\circ$.

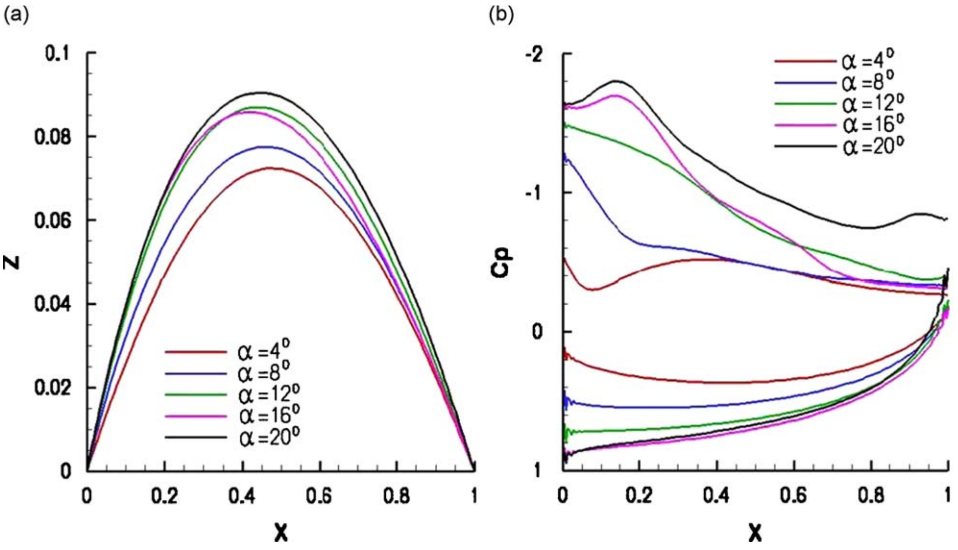

Fig. 3. Mean (a) deflection and (b) surface pressure coefficient for various angles of attack.

membrane airfoil performance. As the angle of attack is raised to $\alpha = 8^\circ$ the downstream separation point moves upstream to $x = 0.57$ and the normal extent of the separation bubble increases. The upstream separation bubble also increases in size with attachment occurring at $x = 0.161$. By $\alpha = 12^\circ$ the two separation zones are merging creating one large separation region that is narrow in vertical extent and covers nearly the full length of the airfoil. At $\alpha = 16^\circ$ the separation zone has shrunk with attachment at $x = 0.774$, but the normal extent of the separated region has grown. By $\alpha = 20^\circ$ a massively separated flow region exists over the airfoil. A small secondary separation region has also developed at the leading edge of the membrane.

A corresponding behavior is noted in the contours of mean vorticity, Figs. 2(a–e). At the lowest angle of attack, Fig. 2(a), the shear layer separates from the upstream mount but rapidly attaches to the membrane airfoil. It subsequently departs from the membrane surface downstream at the previously noted separation location. By $\alpha = 12^\circ$, Fig. 2(c), the shear layer separates from the upstream mount and never reattaches to the membrane surface with a notable thickening of the shear layer observed. At the higher angles of attack the departure angle of the shear layer from the leading edge mount grows and the shear layer moves increasingly away from the membrane surface. At the highest angle of attack, Fig. 2(e), a small region of vorticity of the opposite sign is located under the shear layer in the leading edge region associated with the development of the secondary separation region.

The resulting mean surface pressure distributions on the membrane are plotted in Fig. 3(b). As the incidence angle increases a strong suction peak develops in the leading edge region associated with the strengthening of the upstream separated vortical flow. The extent of this low pressure zone lengthens with a more gradual pressure recovery over the airfoil at higher angles of attack. On the lower surface the pressure progressively increases as the angle of attack is raised.

Shown in Fig. 4 is a comparison of the mean lift coefficient for the flexible membrane airfoil, as well as for a rigid flat airfoil. The C_L distribution for a symmetric airfoil based on thin-airfoil theory is also shown for reference purposes. The rigid airfoil lift coefficient increases approximately in a linear fashion with a slope which is close to the theoretical value. A maximum C_L is achieved for $\alpha = 12^\circ$. Beyond this angle of attack, the lift distribution displays the characteristics of a stalled flow. The flexible membrane airfoil exhibits a lift variation which differs significantly from its rigid counterpart. At zero incidence, a significant lift is achieved due to the camber effect induced by flexibility. As the angle of attack is increased up to $\alpha = 12^\circ$, C_L increases in an approximately linear fashion albeit with a reduced slope relative to either the rigid case or the theoretical distribution. For higher incidence ($12^\circ < \alpha < 20^\circ$), the flexible airfoil lift coefficient continues to rise, although there is a further reduction in the lift-curve slope. Therefore, at high angles of attack, airfoil flexibility results in substantial lift enhancement relative to the rigid case. For the range of α considered, there appears to be no evidence of stall for the membrane airfoil, at least in terms of the aerodynamic lift coefficient. Lift enhancement due to wing flexibility at high angles of attack has also been demonstrated in wind tunnel tests by Waszak et al. (2001) and Song et al. (2008). This enhanced lift is due to both the effect of the induced mean camber as well as the dynamic surface motion to be described next.

5.1.2. Unsteady response

Instantaneous snapshots (and corresponding animations) of the flow response reveal the changing unsteady flow structure with increasing angle of attack, Fig. 5. At $\alpha = 4°$ the flow separates just past the midpoint of the airfoil.

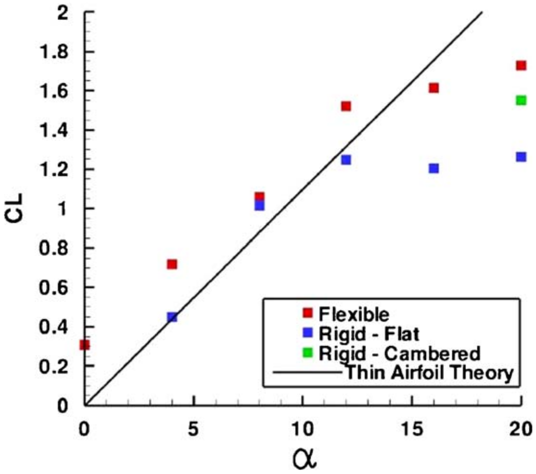

Fig. 4. Comparison of mean lift coefficient for a flexible membrane wing, rigid flat airfoil and a rigid cambered airfoil.

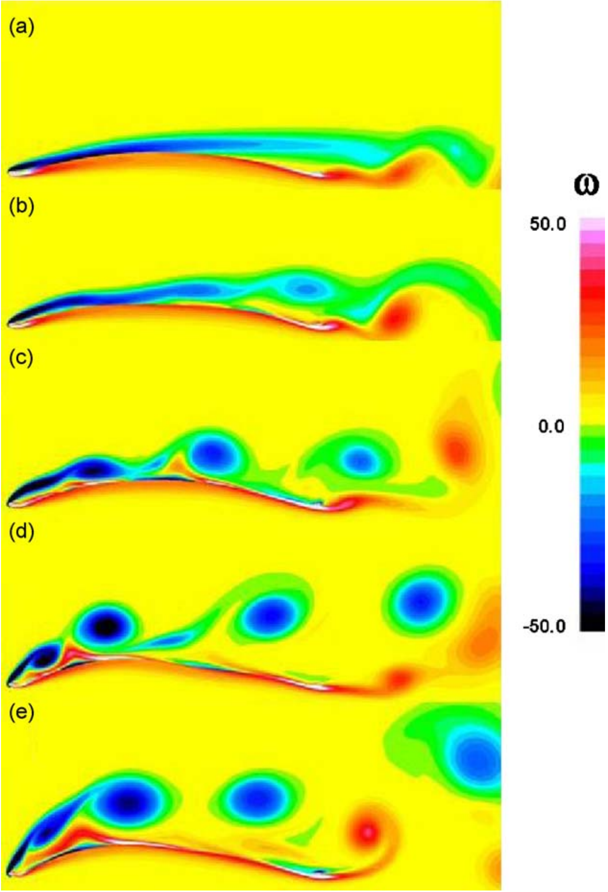

Fig. 5. Instantaneous vorticity for various angles of attack: (a) $\alpha = 4°$, (b) $\alpha = 8°$, (c) $\alpha = 12°$, (d) $\alpha = 16°$, (e) $\alpha = 20°$.

The separated shear layer does not become unstable and roll up until it passes the trailing edge where it interacts with the separating flow from the lower surface, however. Therefore, the flow over the airfoil is predominantly steady. As the angle of attack is increased the flow becomes increasingly unsteady over the airfoil, with the onset of the instability and roll up of the shear layer moving progressively upstream. Up to $\alpha = 12^\circ$ the vortices that form and propagate downstream remain close to the airfoil surface. At the higher angles of attack, $\alpha = 16^\circ$ and 20°, the vortex train tends to depart from the airfoil surface downstream. As the individual vortices form and strengthen, they interact with the surface boundary layer, resulting in the development of secondary vortices of the opposite sign and the eventual eruption of vorticity of the opposite sign from the surface. Pairing of the shear layer vortices is also observed at the higher angles of incidence.

The unsteady structural response of the membrane airfoil is shown in Fig. 6. This figure displays the membrane oscillations by means of $x-t$ diagrams showing the difference between the instantaneous and mean membrane deflection. The membrane is nominally stationary at $\alpha = 4^\circ$ since, as noted earlier, the flow is steady over the major portion of the airfoil (Fig. 5(a)). At $\alpha = 8.0^\circ$, a third mode standing wave response develops. At the higher angles of attack, $\alpha = 12-20^\circ$, the membrane structural response exhibits a less regular behavior resulting from a combination of

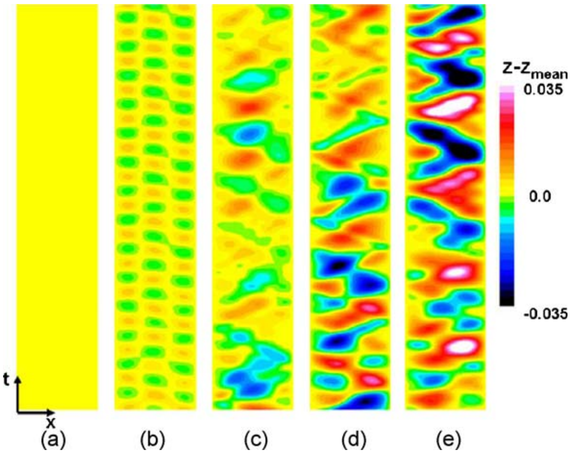

Fig. 6. $x-t$ diagram for perturbation from the mean membrane deflection for various angles of attack: (a) $\alpha = 4^\circ$, (b) $\alpha = 8^\circ$, (c) $\alpha = 12^\circ$, (d) $\alpha = 16^\circ$, (e) $\alpha = 20^\circ$.

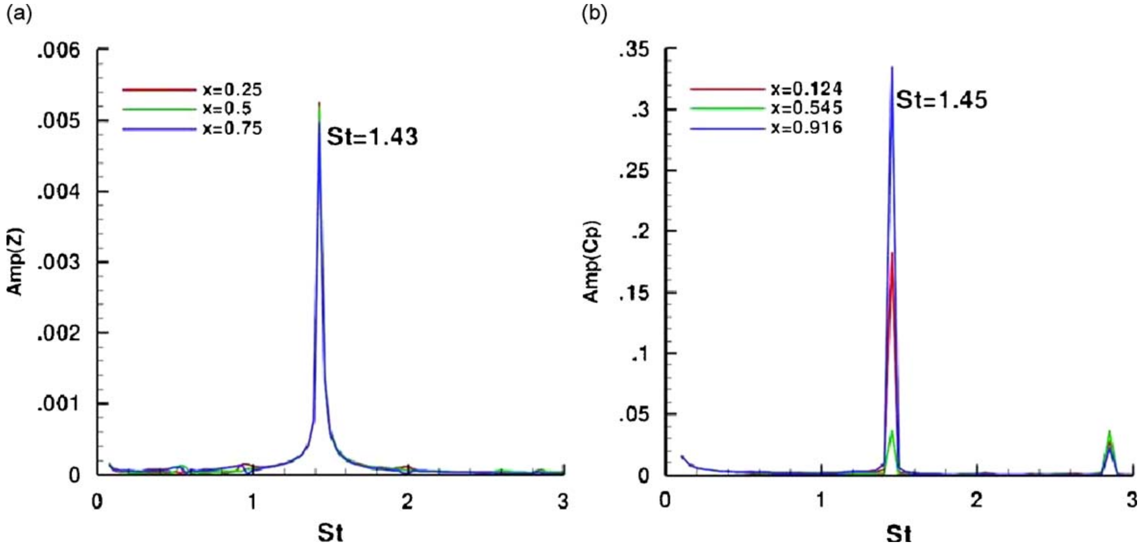

Fig. 7. Spectral analysis of (a) structural response and (b) vortex shedding for $\alpha = 8^\circ$.

structural modes. The maximum peak-to-peak amplitude of the deflection grows with increasing angle of attack reaching values of order $0.07c$ which is of the same order as the maximum mean deflection (Fig. 3(a)).

A spectral analysis of the membrane fluctuations was performed for each angle of attack at chordwise locations of $x = 0.25$, 0.5, and 0.75. In addition, spectral analyses of the pressure fluctuations at chordwise locations above the airfoil by which the shed vortices are passing are also made. At $\alpha = 8^\circ$, where the membrane exhibited a third mode standing wave, Fig. 6(b), a single dominant frequency is observed both in the structural, Fig. 7(a), and vortex shedding, Fig. 7(b). These frequencies correlate to within the tolerance of the Fourier analysis performed. At the higher angles of attack, $\alpha = 12{-}20^\circ$, where the less regular structural vibration occurs, multiple frequency peaks are observed in the structural response. By $\alpha = 20^\circ$, three peaks are observed in the structural analysis, Fig. 8(a), with corresponding peaks in the computed vortex shedding frequencies. The dominant structural frequency, $\mathrm{St} = 0.59$ correlates with the vortex shedding frequency, $\mathrm{St} = 0.6$. This frequency corresponds with the standard value for the wake shedding frequency when rescaled by angle of attack, $\mathrm{St}\,\sin(\alpha) = 0.2$. This observation is consistent with the experimental measurements reported by Rojratsirikul et al. (2008).

Table 2 presents a summary of the spectral analysis results as well as the values of the linear model frequencies computed using the mean membrane tension with the following relation, $\mathrm{St} = \frac{1}{2}n\sqrt{T/\rho_s h}$. At each angle of attack there is a strong correlation between the measured structural frequencies and the vortex shedding frequency. This indicates

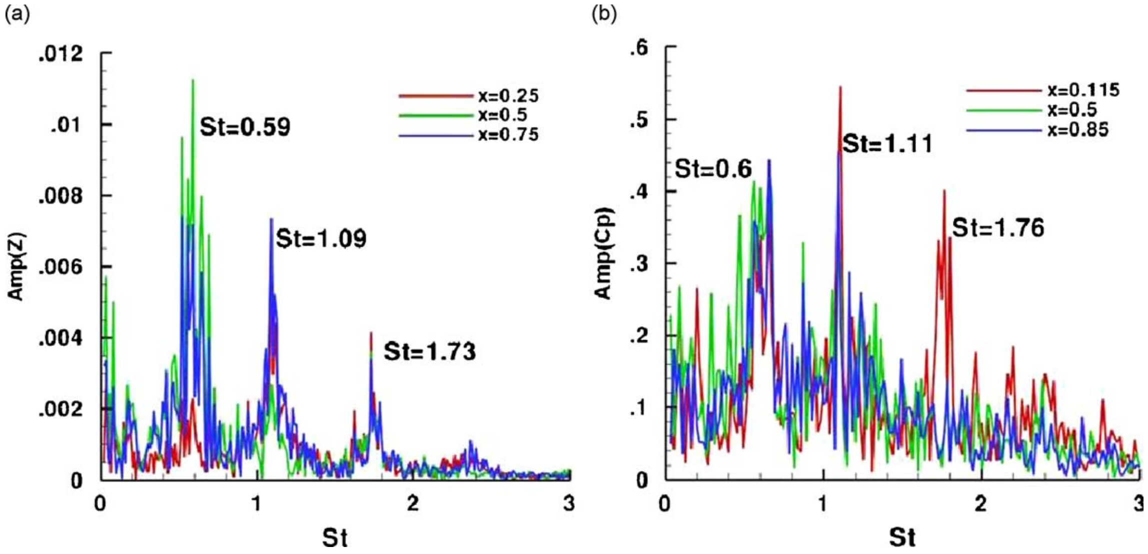

Fig. 8. Spectral analysis of (a) structural response and (b) vortex shedding for $\alpha = 20^\circ$.

Table 2
Vortex shedding frequencies, structural response frequencies and linear model frequencies.

α	Eh	δ_0	Re	Vortex shedding			Structural response			Linear model		
				St_1	St_2	St_3	St_1	St_2	St_3	St_1	St_2	St_3
8	50	0.0	2500	1.45	****	****	1.43	****	****	0.58	1.16	1.74
12	50	0.0	2500	0.87	****	****	0.48	0.86	****	0.66	1.32	1.98
16	50	0.0	2500	0.60	1.02	****	0.58	1.10	****	0.66	1.32	1.98
20	50	0.0	2500	0.60	1.11	1.76	0.59	1.09	1.73	0.66	1.32	1.98
8	25	0.0	2500	1.50	****	****	1.53	****	****	0.55	1.10	1.65
8	100	0.0	2500	1.10	****	****	1.07	****	****	0.64	1.28	1.92
8	50	0.01	2500	1.04	****	****	1.04	****	****	0.645	1.29	1.935
8	50	0.02	2500	1.16	****	****	1.15	****	****	0.73	1.46	2.19
8	50	0.0	5000	1.47	2.91	****	1.43	****	****	0.61	1.22	1.83
8	50	0.0	10 000	1.56	2.72	****	1.56	****	****	0.62	1.24	1.86

a close coupling between the dynamic structural response and the unsteady vortex shedding above. For $\alpha = 8^\circ$, where a clear third mode structural response was noted, the structural frequency falls between the second and third linear model frequencies. At higher angles of attack no clear correlation between the computed frequencies for this nonlinear problem and the linear model frequencies is noted.

In order to separate the effects of the dynamic motion of the membrane from the mean induced camber at higher angles of attack, a computation was run at $\alpha = 20^\circ$ for a rigid cambered airfoil with its shape prescribed by the previously computed mean membrane deflection. A comparison of the mean and unsteady solutions for these two cases is shown in Fig. 9. Comparing the mean solution for the rigid, Figs. 9(a, d), and the dynamic, Figs. 9(b, e), cases shows that the rigid flowfield exhibits a larger and stronger stall vortex and a larger secondary separation bubble located further downstream on the airfoil between $x = 0.171$ and 0.44. There is also a strong region of vorticity of the opposite sign near the trailing edge region, associated with the roll up of a vortex from the trailing edge. These significant differences between the time-averaged flows for the rigid and flexible airfoils result from a distinct change in the instantaneous vortical structure, Figs. 9(f, g). The dynamic motion of the membrane excites the shear layer separating at the leading edge causing it to roll up sooner and to form a series of more coherent vortices which convect closer to the airfoil surface, Fig. 9(g). The trailing edge vortex in the dynamic case is also reduced in strength and forms farther downstream and away from the airfoil. A similar comparison between rigid (cambered) and flexible membrane airfoils has been investigated experimentally by Rojratsirikul et al. (2008). Their flow visualizations also illustrate a reduction of the separation zone due to the dynamic motion of the membrane.

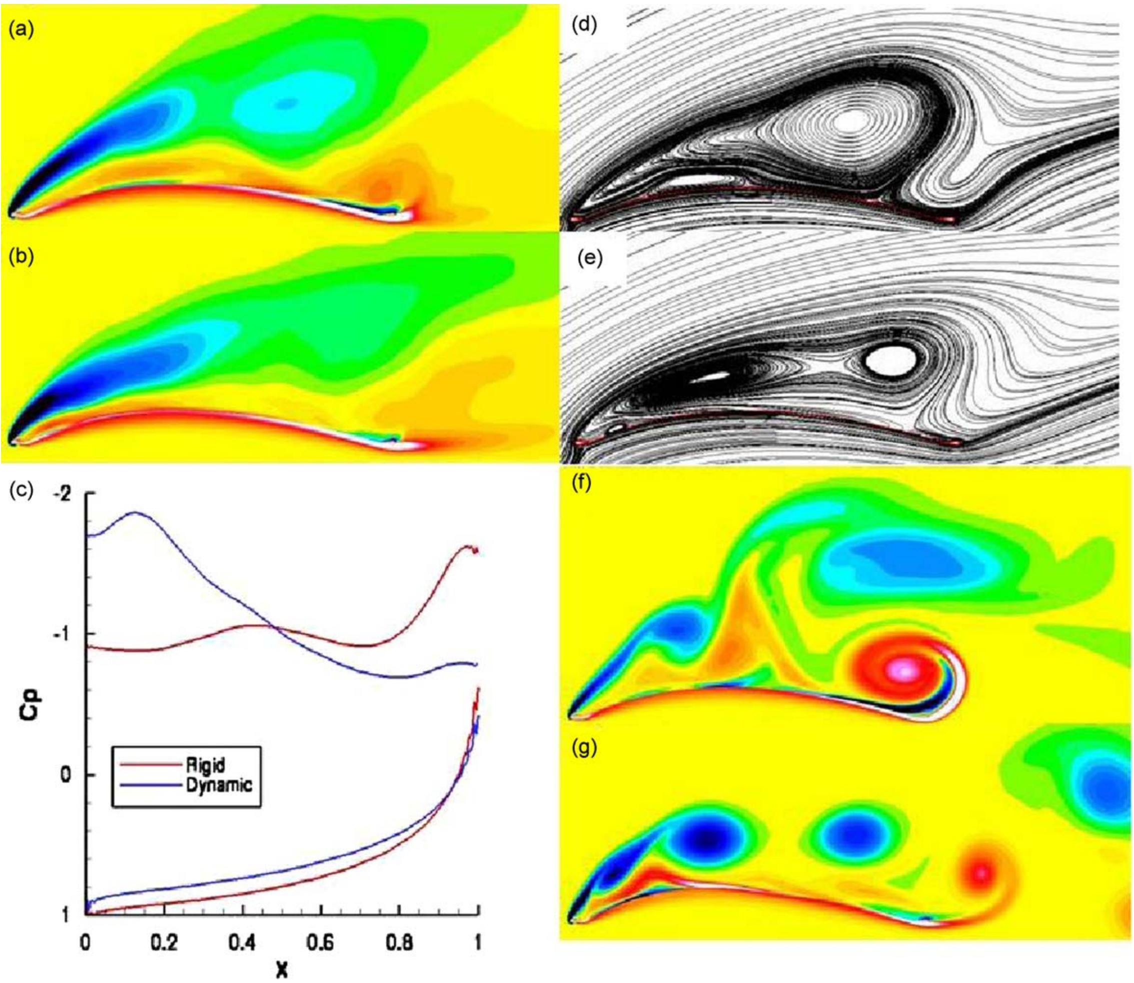

Fig. 9. Comparison of (a, d, f) the rigid and (b, e, g) dynamic membrane airfoil solutions for $\alpha = 20^\circ$: (a, b) mean vorticity, (d, e) mean streamlines, (c) surface pressure coefficient, (f, g) instantaneous vorticity.

These changes in the flowfield lead to very different mean pressure distributions around the airfoil Fig. 9c. This is particularly true on the upper surface where the rigid case exhibits a very flat pressure distribution characteristic of a fully stalled flow except near the trailing edge where the influence of the trailing edge vortex is observed. In contrast, the dynamic case shows a strong suction region over the front portion of the wing but higher values of pressure downstream. This change in pressure distribution results in a switch from a nose down moment in the rigid case to a nose up moment for the elastic case. The overall impact of flexibility, through the combined effects of induced mean camber and dynamic motion, is a significant delay in the stall of the airfoil with a corresponding increase in lift coefficient in the post-stall region (Fig. 4). This enhanced lift arises predominantly from the effect of mean camber with additional lift enhancement resulting from the membrane motion. Further investigation of the impact of the dynamic structural response on the overall aerodynamics is warranted, as it may provide a means for passively controlling the flow to provide improved airfoil performance through judicious aeroelastic tailoring.

5.2. *Effect of membrane rigidity*

5.2.1. *Mean response*

The impact of the elasticity of the membrane material can be analyzed by varying the structural parameter, *Eh*, which is the nondimensional modulus of elasticity times the thickness of the membrane. Baseline flow conditions, $\alpha = 8^\circ$ and $\mathrm{Re} = 2500$ are considered. Increasing the rigidity of the membrane decreases the overall mean camber, Fig. 10. The maximum deflection of the membrane is notably reduced from $z = 0.104$ for $Eh = 25$ to $z = 0.06$ for $Eh = 100$, Fig. 11(a). The effect of this change in shape on the mean flow, Fig. 10, is to decrease the size and strength of the

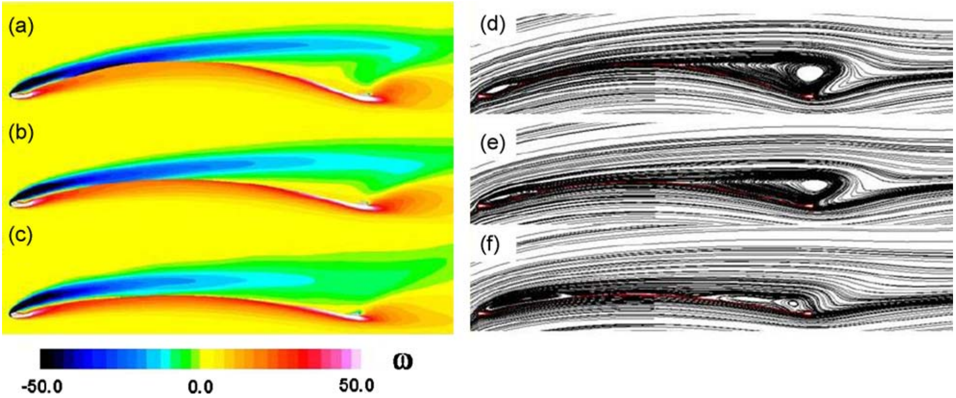

Fig. 10. Mean vorticity and streamline patterns for increasing values of *Eh*: (a, d) $Eh = 25$, (b, e) $Eh = 50$, (c, f) $Eh = 100$.

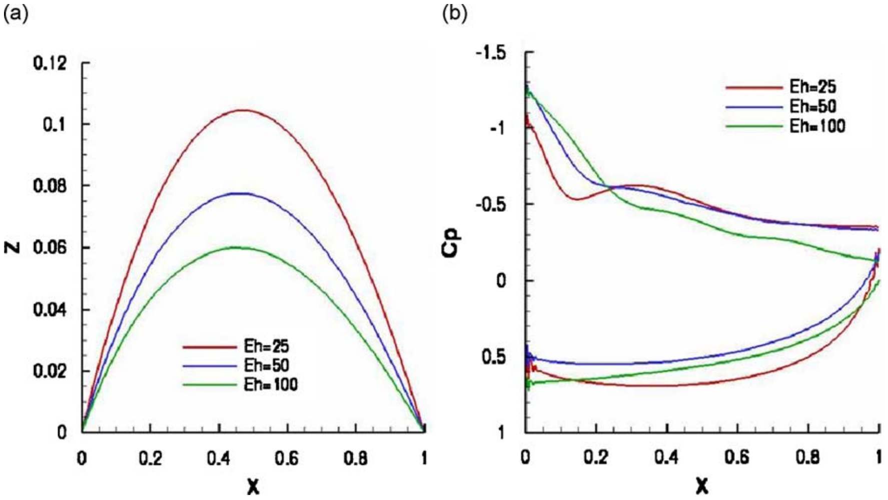

Fig. 11. Mean (a) deflection and (b) surface pressure coefficient for increasing membrane rigidity.

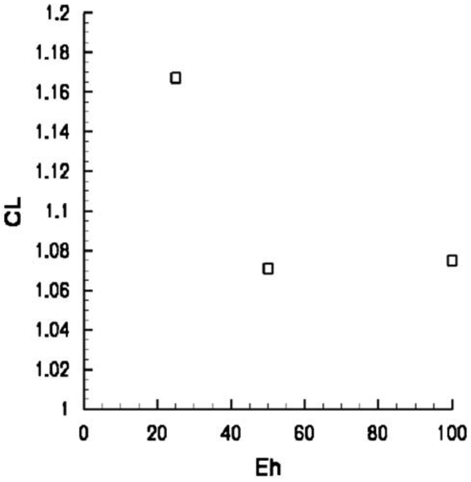

Fig. 12. Effect of membrane rigidity on mean lift coefficient.

downstream separated flow moving the mean separation point from $x = 0.574$ for $Eh = 25$ to $x = 0.726$ for $Eh = 100$. Alternately, the leading edge separation bubble grows and strengthens with the attachment point moving downstream from $x = 0.103$ to 0.287.

The lift coefficient, Fig. 12, decreases when the membrane rigidity is increased from $Eh = 25$ to 50. Interestingly, little further change results when increasing to $Eh = 100$. The reason for this can be seen in Fig. 11(b) which displays the mean pressure coefficients for each value of Eh. As Eh is increased from 25 to 50, a pressure loss is seen on the lower surface over the full extent of the airfoil. On the upper surface the pressure stays nominally the same over the aft 75% of the airfoil while the enhanced suction near the leading edge is offset by the decreased pressure on the lower surface. Therefore, a net loss in lift results. As the rigidity is increased further from 50 to 100, there is a loss in suction on the upper surface associated with the weaker downstream separation which is offset by an increase in pressure on the lower surface and enhanced suction towards the leading edge where the separated flow is strengthening. In contrast to the present results, inviscid, thin airfoil theory would suggest a continuing decrease in lift with decreasing camber. The differences with inviscid, thin airfoil theory indicate that viscous effects at these low Reynolds numbers as well as the dynamic response to be described next play a significant role in determining the lift response.

5.2.2. Unsteady response

The ramifications of increasing membrane rigidity on the unsteady response is shown in Fig. 13. For the most flexible membrane, the attached boundary layer separates just beyond the midpoint of the airfoil, but does not roll up and become unsteady until it passes the trailing edge and interacts with the separating flow from the underside of the airfoil. As the membrane is stiffened and the size of the deflection decreases, the flow becomes increasingly unsteady with the vortex roll up moving progressively upstream. The shed vortices are stronger and more coherent for $Eh = 100$. Measured values of the vortex shedding frequency for each value of the membrane rigidity are given in Table 2. The shedding frequency decreases with increasing membrane rigidity.

The dynamic structural response of the membrane also changes with increasing membrane rigidity, Fig. 14. Due to the close coupling of the membrane dynamics with the unsteady vortex dynamics, the frequency of the membrane response drops in accordance with the decrease in vortex shedding frequency (see Table 2). For $Eh = 25$ and 50, the membrane vibrates in the third mode with increasing amplitude as the unsteady vortex shedding moves upstream over the airfoil. As the rigidity is increased further to $Eh = 100$ and the frequency of the structural response decreases due to the lower vortex shedding frequency, the membrane response switches from third mode to second mode. The amplitude of the unsteady response increases even further with the strengthening of the unsteady vortices propagating over the airfoil.

5.3. Effect of membrane pretension

5.3.1. Mean response

Understanding the effect of pretension on the membrane airfoil response will be particularly important when comparing computed results with experimental measurements where the amount of pretension in the system may not be

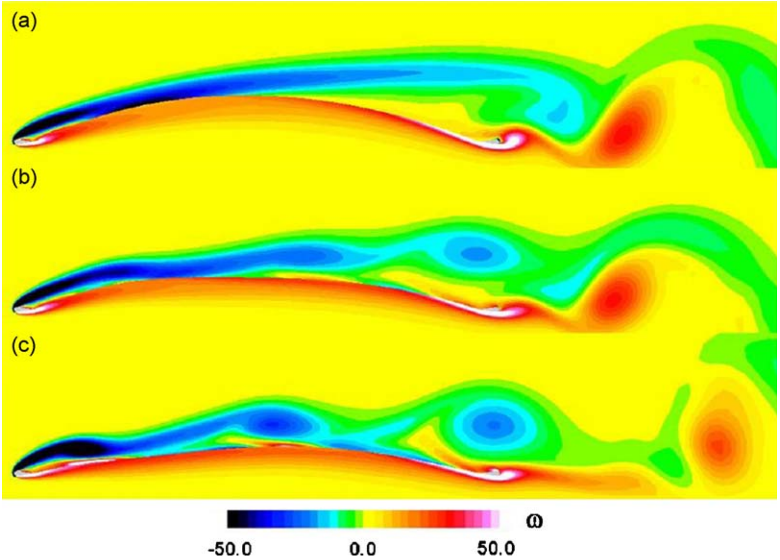

Fig. 13. Instantaneous vorticity for increasing values of *Eh*: (a) $Eh = 25$, (b) $Eh = 50$, (c) $Eh = 100$.

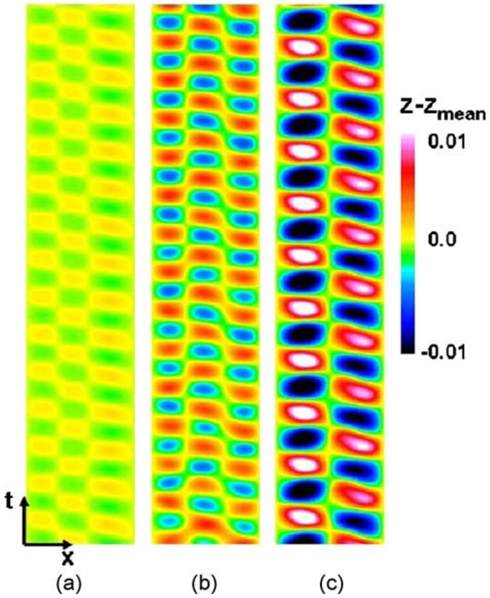

Fig. 14. $x-t$ diagram for perturbation from the mean membrane deflection for increasing values of *Eh*: (a) $Eh = 25$, (b) $Eh = 50$, (c) $Eh = 100$.

known *a priori*. Fig. 15 displays the mean vorticity and streamline patterns for increasing amounts of pretension. As with increasing membrane rigidity, the primary effect is to decrease the amount of induced camber. The maximum deflection reduces from $z = 0.078$ for the case with no pretension to $z = 0.044$ for the case with 2% pretension, Fig. 16(a). As a result of the decreasing camber, the downstream separated flow region is greatly reduced while the upstream separation bubble grows in size and strength. For the 2% pretension case, only a very small separation bubble extending from $x = 0.751$ to 0.923 remains downstream while the upstream attachment point has progressed from $x = 0.274$ for no pretension to $x = 0.327$. Correspondingly, the vorticity downstream weakens and is diffused over a broader area while the vorticity in the leading edge region strengthens.

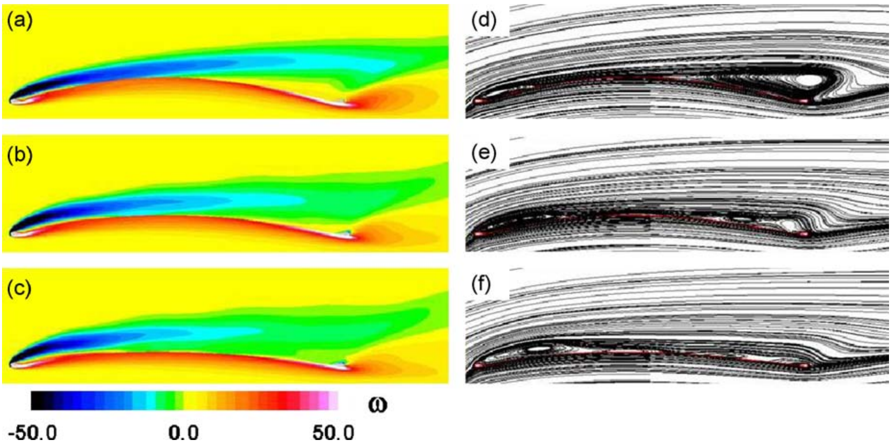

Fig. 15. Mean vorticity and streamline patterns for increasing pretension: (a, d) $\delta_0 = 0.0$, (b, e) $\delta_0 = 0.01$, (c, f) $\delta_0 = 0.02$.

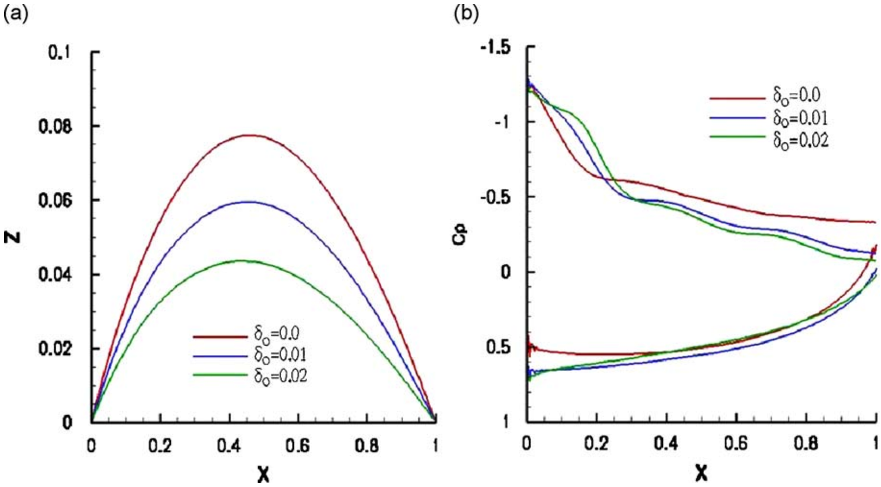

Fig. 16. Mean (a) deflection and (b) surface pressure coefficient for increasing pretension.

Fig. 17 presents the overall impact on the lift coefficient. As with increasing membrane rigidity, the change in lift coefficient does not follow the inviscid, thin airfoil trends due to the importance of viscous and dynamic effects. The influence of the changing flow pattern on the upper surface pressure coefficient is observed in Fig. 16(b). There is a growing suction region at the leading edge associated with the strengthening of the mean vortical flow upstream. Over the aft portion of the airfoil there is an increase in pressure on the upper surface as the large separated region disappears. Changes on the lower surface are less distinct, though there is a clear rise in pressure at the leading edge for the two cases with pretension.

5.3.2. *Unsteady response*

The development of the unsteady flowfield as the pretension is increased is exhibited in Fig. 18. The unsteady flowfield is characterized by the formation and shedding of vortical structures from the leading edge. As the pretension is increased, this unsteady process is enhanced with the shed vortices strengthening and becoming more distinct. The shedding frequency, Table 2, shows a marked drop from $\mathrm{St} = 1.45$ for no pretension to $\mathrm{St} = 1.04$ for 1% pretension and $\mathrm{St} = 1.16$ for 2% pretension.

Fig. 19 plots $x{-}t$ diagrams of the perturbation from the mean deflection to highlight the membrane structural response. For no pretension a third mode standing wave is observed with a frequency $\mathrm{St} = 1.43$. With the addition of pretension, the dominant mode changes to the second mode and a drop in the frequency of vibration is observed.

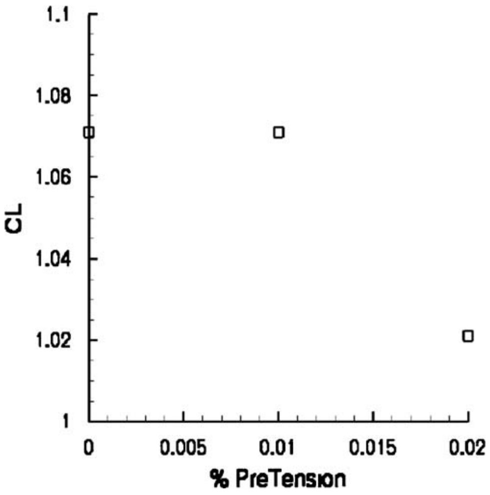

Fig. 17. Effect of pretension on mean lift coefficient.

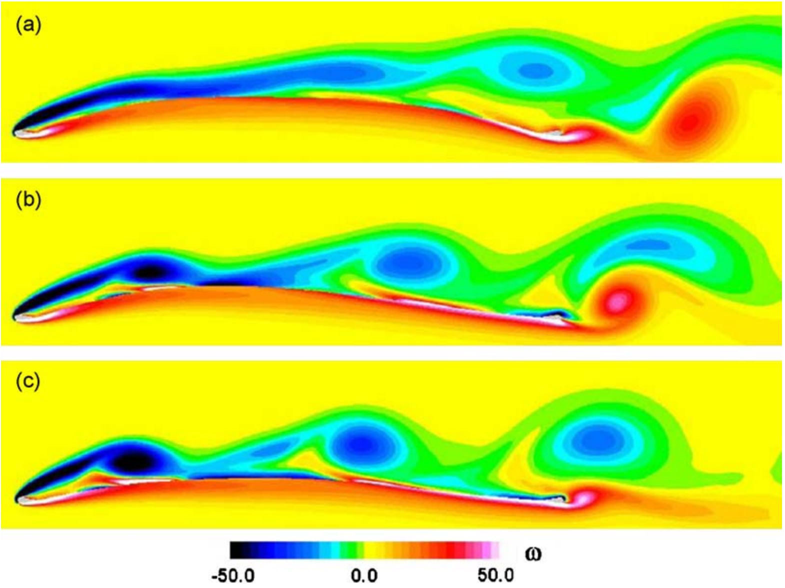

Fig. 18. Instantaneous vorticity for increasing pretension: (a) $\delta_0 = 0.0$, (b) $\delta_0 = 0.01$, (c) $\delta_0 = 0.02$.

For 1% pretension the frequency is $\mathrm{St} = 1.04$ while for 2% pretension $\mathrm{St} = 1.15$. While a drop in the structural frequency with increasing pretension is counterintuitive, the structural response is again being driven by the close coupling of the unsteady vortical flow and the structural response.

5.4. Effect of Reynolds number

5.4.1. Mean response

Increasing Reynolds number can also meaningfully alter the membrane response and the corresponding flowfield at these low Reynolds numbers. Fig. 20 shows the effect of increasing Reynolds number on the overall flow structure. Doubling the Reynolds number from $\mathrm{Re} = 2500$ to 5000 increases the maximum membrane deflection from $z = 0.0775$ to 0.0815 (see Fig. 21(a)). An enhanced separated flow region develops upstream with the attachment point shifting from $x = 0.161$ to 0.226. The downstream separation zone is significantly reduced with the separation point moving

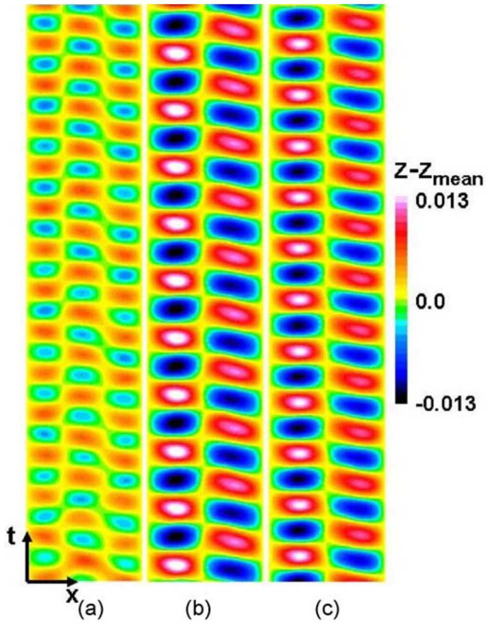

Fig. 19. $x-t$ diagram for perturbation from the mean membrane deflection for increasing pretension: (a) $\delta_0 = 0.0$, (b) $\delta_0 = 0.01$, (c) $\delta_0 = 0.02$.

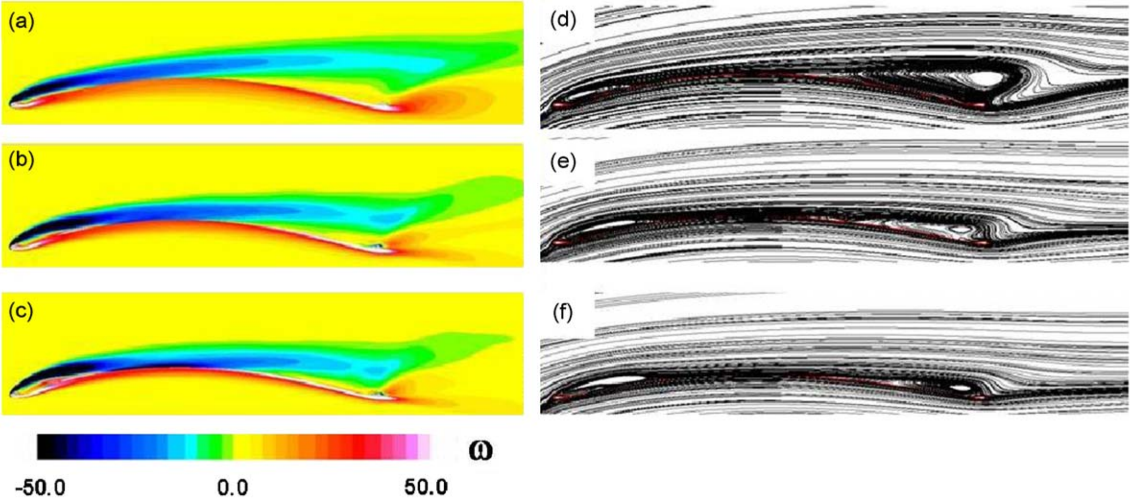

Fig. 20. Mean vorticity and streamline patterns for increasing Reynolds number: (a, d) Re = 2500, (b, e) Re = 5000, (c, f) Re = 10 000.

from $x = 0.574$ to 0.738. A further increase in Reynolds number to Re = 10 000 does not greatly affect the mean deflection. The upstream separated flow region is strengthened but does not grow further in size. A secondary separation bubble with associated vorticity of the opposite sign is also noted underneath the primary separation bubble, Figs. 20(c, f). The downstream separation is further reduced in size and strength.

The imprint of the strengthening vortical flow at the leading edge of the airfoil is very apparent in the surface pressure coefficient, Fig. 21(b). At the two higher Reynolds numbers a low pressure region over the first 25% of the airfoil results from the increasing strength of the separation bubble above. Higher values of pressure are also obtained on the lower surface for the two larger Reynolds number flows. As a result of the these changes in the flowfield structure, the lift coefficient is enhanced with increasing Reynolds number, Fig. 22.

5.4.2. Unsteady response

Fig. 23 demonstrates the impact of Reynolds number on the unsteady flow response over the membrane airfoil. For the lower two Reynolds numbers the flow is characterized by the regular formation and shedding of vortical structures from the leading edge which travel over the surface of the airfoil. These vortical structures are stronger and more distinct for Re = 5000. The magnitude of the dominant vortex shedding frequency increased slightly at Re = 5000, Table 2, and peaks at higher frequencies are present in the spectrum. The spectrum remains clean as for Re = 2500 (Fig. 7(b)), however, with only very distinct frequency peaks occurring. At Re = 10 000, the flow becomes much more complex with the shed vortices undergoing pairings and complex interactions with the surface boundary layer. While distinct peaks still exist in the spectrum at this Reynolds number, the content of the spectrum is much richer, with energy being distributed over a broad range of frequencies. This may be indicative of the breakdown of the two-dimensional, laminar flow assumption for this Reynolds number and the need for three-dimensional simulations not considered in the present work.

The dynamic structural response produced is shown in Fig. 24. The two lower Reynolds number cases show a regular third mode standing wave. The frequency of the structural vibration in these two cases correlates well with the vortex shedding frequency, Table 2, again indicating a close coupling between the fluid and structural dynamics. At the highest Reynolds number there is a clear change in the character of the structural motion. A dominant mode is difficult to discern and the response appears to have more of a traveling wave rather than a standing wave nature. In the spectral

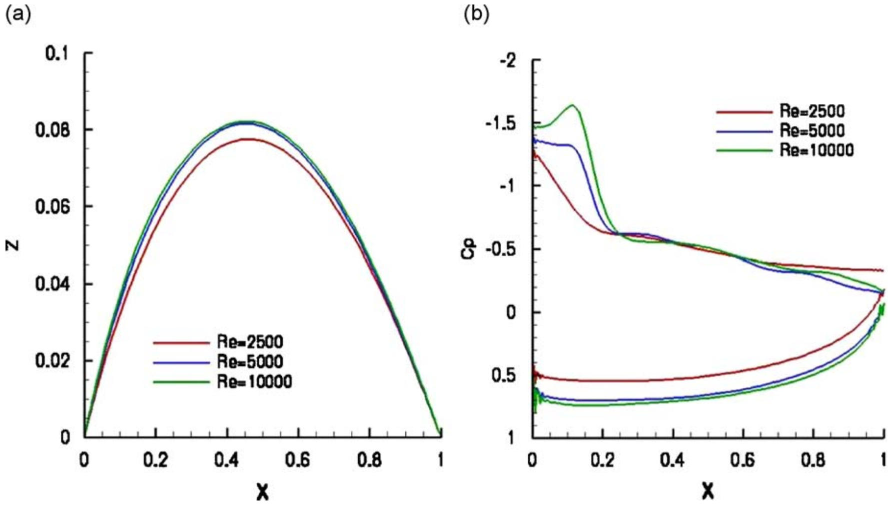

Fig. 21. Mean (a) deflection and (b) surface pressure coefficient for increasing Reynolds number.

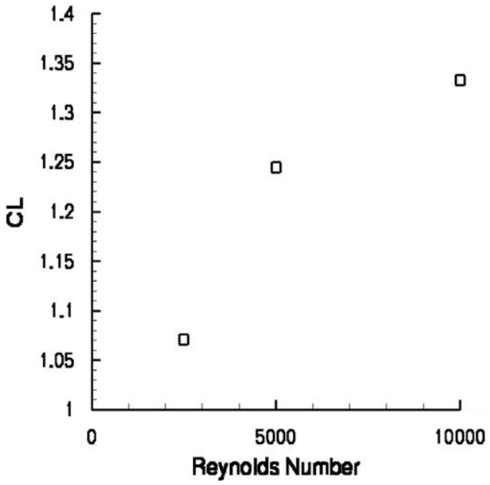

Fig. 22. Effect of Reynolds number on mean lift coefficient.

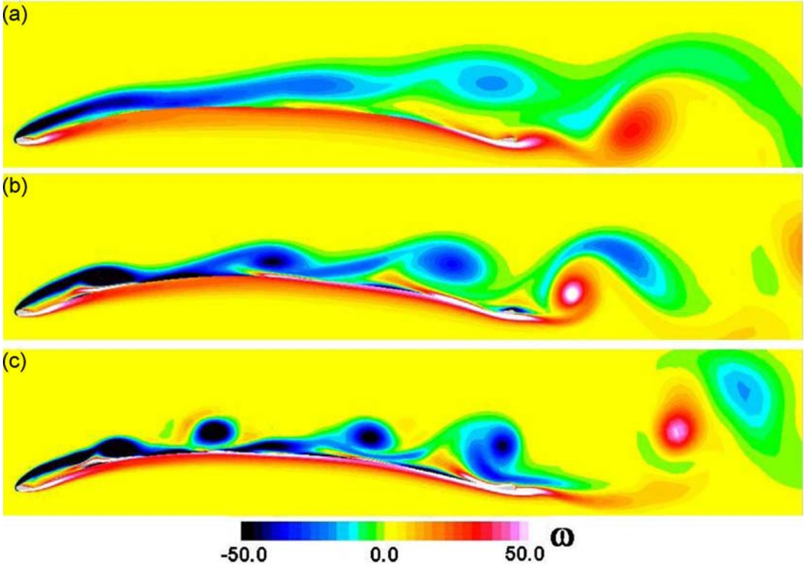

Fig. 23. Instantaneous vorticity for increasing Reynolds number: (a) Re = 2500, (b) Re = 5000, (c) Re = 10 000.

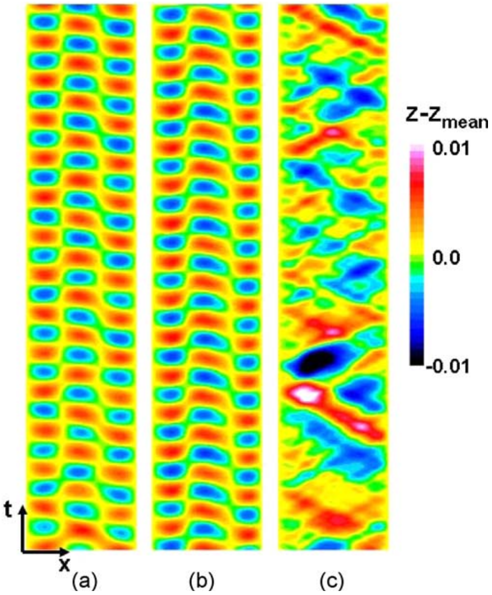

Fig. 24. $x-t$ diagram for perturbation from the mean membrane deflection for increasing Reynolds number: (a) Re = 2500, (b) Re = 5000, (c) Re = 10 000.

analysis a dominant structural frequency is still seen that correlates with the vortex shedding frequency, but energy is also distributed over a range of frequencies lower than the dominant frequency.

6. Conclusions

A well-validated, robust, sixth-order Navier–Stokes solver has been coupled with a nonlinear membrane structural model to computationally investigate flexible membrane airfoils. The aerodynamic and structural solvers are tightly coupled through a subiterative process which provides a complete synchronization of the fluid and structural solvers. Computations have been performed for a two-dimensional membrane wing airfoil. The effect of angle of attack, membrane rigidity, membrane pretension and Reynolds number on the mean and unsteady response of the flexible membrane airfoil was described.

The most notable effect of the membrane flexibility is the introduction of a mean camber to the membrane airfoil. A close coupling between unsteady vortex shedding and the dynamic structural response has also been demonstrated. Dynamic motion of the membrane surface significantly alters the unsteady flow over the membrane airfoil at high angles of attack. The coupling of this dynamic effect and the mean camber results in a delay in stall with a corresponding improvement in mean lift.

Increasing membrane rigidity or alternatively introducing membrane pretension resulted in a reduction of the mean camber of the airfoil. This change in camber produces an increasingly unsteady flow, albeit with a reduced frequency for the vortex shedding. This reduction in the vortex shedding frequency correlates with a reduction in frequency of the structural vibrations and a shift from a third mode to second mode response.

Increasing the Reynolds number from $\mathrm{Re} = 2500$ to 10 000 engendered an increase in the mean deflection of the airfoil and an increasingly complex and unsteady flow response. For the two lower Reynolds numbers the membrane exhibited a very regular third mode vibratory response which was closely coupled to the vortex shedding process over the airfoil. As the Reynolds number was increased further, the structural response underwent a distinct change in character from a standing wave vibration to a dynamic character that was more of a traveling wave nature. The character of the unsteady vortex flow also became much more chaotic. This may be an indication of the breakdown of the two-dimensional, laminar flow assumption at the highest Reynolds number and the onset of transitional flow which is not captured. Further computations beyond the scope of the present work will be needed to resolve this question.

Acknowledgments

This work was sponsored by AFOSR under a task monitored by Lt. Col. Rhett Jefferies and supported in part by a grant of HPC time from the DoD HPC Shared Resource Center at the Air Force Research Laboratory. The author would also like to acknowledge several useful discussions with his colleague Dr Miguel Visbal.

References

Alpert, P., 1981. Implicit filtering in conjunction with explicit filtering. Journal of Computational Physics 44, 212–219.

Anderson, D., Tannehill, J., Pletcher, R., 1984. Computational Fluid Mechanics and Heat Transfer. McGraw-Hill Book Company, New York.

Attar, P.J., Gordnier, R.E., 2006. Aeroelastic prediction of the limit cycle oscillations of a cropped delta wing. Journal of Fluids and Structures 22, 45–58.

Beam, R., Warming, R., 1978. An implicit factored scheme for the compressible Navier–Stokes equations. AIAA Journal 16 (4), 393–402.

Gaitonde, D., Shang, J., Young, J., 1997. Practical aspects of high-order accurate finite-volume schemes for electromagnetics. AIAA Paper 97-0363.

Gaitonde, D., Visbal, M., 1998. High-order schemes for Navier–Stokes equations: algorithm and implementation into FDL3DI. Technical Report AFRL-VA-WP-TR-1998-3060, Air Force Research Laboratory, Wright-Patterson AFB.

Gaitonde, D., Visbal, M., 1999. Further development of a Navier–Stokes solution procedure based on higher-order formulas. AIAA Paper 99-0557.

Gordnier, R.E., Visbal, M.R., 2002. Development of a three-dimensional viscous aeroelastic solver for nonlinear panel flutter. Journal of Fluids and Structures 16, 497–527.

Gordnier, R.E., Visbal, M.R., 2004. Computation of the aeroelastic response of a flexible delta wing at high angles of attack. Journal of Fluids and Structures 19, 785–800.

Jameson, A., Schmidt, W., Turkel, E., 1981. Numerical solutions of the euler equations by a finite volume method using Runge–Kutta time stepping schemes. AIAA Paper 81-1259.

Le Maitre, O., Huberson, S., Souza De Cursi, E., 1999. Unsteady model of sail and flow interaction. Journal of Fluids and Structures 13, 37–59.

Lele, S., 1992. Compact finite difference schemes with spectral-like resolution. Journal of Computational Physics 103, 16–42.

Melville, R.B., Morton, S.A., Rizzetta, D.P., 1997. Implementation of a fully-implicit, aeroelastic Navier–Stokes solver. AIAA 97-2039.

Newman, B.G., 1987. Aerodynamic theory for membranes and sails. Progress in Aerospace Sciences 24, 1–27.

Newman, B.G., Païdoussis, M.P., 1991. The stability of two-dimensional membranes in streaming flow. Journal of Fluids and Structures 5, 443–454.

Persson, P.-O., Peraire, J., Bonet, J., 2007. A high order discontinuous Galerkin method for fluid–structure interaction. AIAA-2007-4327.

Pulliam, T., 1986. Artificial dissipation models for the Euler equations. AIAA 24 (12), 1931–1940.

Pulliam, T., Chaussee, D., 1981. A diagonal form of an implicit approximate-factorization algorithm. Journal of Computational Physics 39 (2), 347–363.

Rojratsirikul, P., Wang, Z., Gursul, I., 2008. Unsteady aerodynamics of membrane airfoils. AIAA-2008-0613.

Shyy, W., Ifju, P., Viieru, D., 2005. Membrane wing-based micro air vehicles. Applied Mechanics Reviews 58, 283–301.

Shyy, W., Smith, R., 1997. A study of flexible airfoil aerodynamics with application to micro aerial vehicles. AIAA-1997-1933.

Smith, R., Shyy, W., 1995. Computation of unsteady laminar flow over a flexible two-dimensional membrane wing. Physics of Fluids 7 (9), 2175–2184.

Song, A., Tian, X., Israeli, E., Galvao, R., Bishop, K., Swartz, S., Breuer, K., 2008. The aero-mechanics of low aspect ratio compliant membrane wings with applications to animal flight. AIAA-2008-0517.

Song, A.J., Breuer, K.S., 2007. Dynamics of a compliant membrane as related to mammalian flight. AIAA-2007-0665.

Visbal, M., Gaitonde, D., 1998. High-order accurate methods for unsteady vortical flows on curvilinear meshes. AIAA Paper 98-0131.

Visbal, M., Gaitonde, D., 1999. High-order accurate methods for complex unsteady subsonic flows. AIAA Journal 37 (10), 1231–1239.

Visbal, M., Gaitonde, D., 2001. Very high-order spatially implicit schemes for computational acoustics on curvilinear meshes. Journal of Computational Acoustics 9 (4), 1259–1286.

Visbal, M.R., Gordnier, R.E., 2004. Numerical simulation of the interaction of a transitional boundary layer with a 2-D flexible panel in the subsonic regime. Journal of Fluids and Structures 19, 881–903.

Waszak, M.R., Jenkins, L.N., Ifju, P., 2001. Stability and control properties of an aeroelastic fixed wing micro aerial vehicle. AIAA-2001-4005.